Basal Pressure Variations Induced by a Turbulent Flow Over a Wavy Surface

Philippe Claudin[1]*, Michel Louge[2] and Bruno Andreotti[3]

[1]Physique et Mécanique des Milieux Hétérogènes, PMMH UMR 7636 CNRS, ESPCI Paris, PSL Research University, Université de Paris, Sorbonne Université, Paris, France, [2]Sibley School of Mechanical and Aerospace Engineering, Cornell University, Ithaca, NY, United States, [3]Laboratoire de Physique de L'Ecole Normale Supérieure, UMR 8550 CNRS, PSL Research University, Université de Paris, Sorbonne Université, Paris, France

Turbulent flows over wavy surfaces give rise to the formation of ripples, dunes and other natural bedforms. To predict how much sediment these flows transport, research has focused mainly on basal shear stress, which peaks upstream of the highest topography, and has largely ignored the corresponding pressure variations. In this article, we reanalyze old literature data, as well as more recent wind tunnel results, to shed a new light on pressure induced by a turbulent flow on a sinusoidal surface. While the Bernoulli effect increases the velocity above crests and reduces it in troughs, pressure exhibits variations that lag behind the topography. We extract the in-phase and in-quadrature components from streamwise pressure profiles and compare them to hydrodynamic predictions calibrated on shear stress data.

Keywords: pressure modulation, bedforms, sinusoidal topography, linear response, laminar-turbulent transition

1 INTRODUCTION

Most natural flows occur on evolving topography. The resulting hydrodynamic variations are described by a linear theory that Jackson and Hunt [1] developed for wind profiles over low hills. Their work inspired analyses of laminar [2–6] and turbulent [7–18] flows on shallow bedforms, as recently reviewed by Finnigan et al. [19]. Flow modulation associated with fluid-structure interactions also drives the dynamics of wind-driven wave generation at a liquid surface [20, 21], or on compliant thin sheets [22–24], leading to the flag instability when a free end is allowed to flap [25].

Most studies of fluid motion on wavy surfaces have focused on basal shear stress, which drives sediment transport [26]. As Charru et al [27] reviewed, coupling the latter to the Jackson and Hunt theory or its variants [10, 13] explains the formation of erodible objects like sand ripples and dunes, which owe their initial growth to a basal shear stress peaking upstream of the highest elevation.

However, basal pressure is also affected by evolving topography. In porous sand beds, streamwise pressure variations produce an internal flow that drives humidity and microscopic particles below the surface [28]. With strong enough winds, the resulting pore pressure can also relieve part of the bed weight, thereby facilitating the onset of its erosion [29]. At much larger scale, topography-induced pressure variations are important to atmospheric science, especially mountain meteorology [30, 31].

Relatively few experiments conducted in air [29, 32–39], water or other liquids [40–48] flowing over wavy surfaces staged harmonic bedforms with low enough ratio of amplitude ζ and wavelength λ to avoid flow detachment. This has made it difficult to compare data with linear theories predicated on small ζ/λ. As the experiments of Hanratty, et al. [47] have shown, a hydrodynamic anomaly occurs when the flow response to topographical variations transitions from laminar to turbulent

behavior. This phenomenon is at the origin of an instability that carves rippled or scalloped features on surfaces able to sublimize or dissolve into the fluid [49, 50], but that disappears when the bed becomes hydrodynamically rough [51]. Recently, such sublimation ripples have been found at the surface of the Martian north polar cap [52], with a typical wavelength much larger than blue ice ripples found in Antarctica [53], but still proportional to the viscous length ν/u_* [54], based on kinematic viscosity ν and shear velocity u_*. This anomalous hydrodynamic response is also essential to understand how subaqueous or Martian ripples are superimposed on dunes [55], acting as a separation of small and large scale bedforms. Therefore, a question is whether streamwise pressure variations are also subject to such anomalous transition.

When fluid flowing on a flat surface reaches an ascending bedform, the narrowing of streamlines raises speed and decreases static pressure, as predicted by energy conservation in the Bernoulli equation. To leading order, this effect is captured by dimensionless coefficients $\mathcal{A}$ and $\mathcal{C}$, which respectively represent the bedform's role on speed and pressure. Because speed rises when pressure decreases, these coefficients have opposite signs, $\mathcal{A} > 0$ and $\mathcal{C} < 0$. In the "outer region" far above the surface, such energy conservation holds. However, in the closer "inner region", inertia causes fluid flow to lag changes in the bedform, a phenomenon that is captured by dimensionless coefficients $\mathcal{B}$ and $\mathcal{D}$ that are both positive, and respectively represent effects on shear and normal stress. Overall, fluid inertia causes surface shear stress to lead topographical variations with a positive phase $\arctan(\mathcal{B}/\mathcal{A}) > 0$, whereas static pressure lags those changes with $\arctan(\mathcal{D}/\mathcal{C}) < 0$. While others have addressed $\mathcal{A}$ and $\mathcal{B}$ [27, 32, 39], this paper focuses on $\mathcal{C}$ and $\mathcal{D}$. We begin with a summary of the theory, which predicts how C and D depend on the wavenumber $k = 2\pi/\lambda$ of bed oscillations.

Our objective is to review articles reporting pressure measurements on wavy surfaces subject to a turbulent flow. As we will discuss, existing data [29, 36, 37, 47, 56] suggest that the anomalous transition in shear stress may also arise in the pressure response. However, we recognize that the corresponding experiments, which were not designed to address this question, do not support a definitive conclusion. In the context of the anomalous transition, a crucial shortcoming of these experiments is their determination of u_*, which may have been approximate. Because the coupling of surface pressure with porous media is relevant to industrial applications and the formation of geophysical bedforms, we hope that this article will inspire future experiments in the dimensionless wavenumber range $10^{-3} \le k\nu/u_* \le 10^{-1}$, where our theory predicts distinct behavior of $\mathcal{D}$ for rough and smooth walls.

2 TURBULENT FLOW OVER A WAVY BED

Because our main objective is to reanalyze existing data for turbulent flows over wavy beds, this section does not repeat our own derivations of the underlying theory, but rather provides a summary of key quantities and concepts. To account for the hydrodynamic anomaly, the framework of Fourrière, et al. [9, 10]

was recently extended, as detailed in [27, 51]. We examine a turbulent fluid flow along the x direction, unbounded vertically and driven by a shear stress ρu_*^2 imposed far above the bed. Restricting attention to the linear flow response to bed relief, the elevation $Z(x)$ can be decomposed in Fourier modes. Therefore, without loss of generality, we consider a bed profile of the form

$$Z(x) = -\zeta \cos(kx), \tag{1}$$

where $k\zeta$ is a parameter $\ll 1$. From **Eq. 1**, troughs reside at $x = 0 \bmod(2\pi)$. z is the crosswise distance normal to the reference mean bed elevation. We assume invariance in the spanwise direction y that completes the Cartesian coordinate system.

In this framework, hydrodynamics is described by Reynolds-averaged Navier-Stokes equations governing the mean velocity field u_i and pressure p. A first order turbulence closure relates the stress tensor τ_{ij} to the velocity gradient. This closure involves a turbulent kinematic viscosity associated with a mixing length and a mixing frequency representing typical eddy length and time scales [57]. The mixing frequency is given by the strain rate, and the mixing length ℓ depends explicitly on distance from the bed. To account for both the smooth and rough regimes, we adopt a mixing length inspired from van Driest [58].

$$\ell = \kappa(z + r \times d - Z)\left\{1 - \exp\left[-\frac{(z + s \times d - Z)\sqrt{\tau_{xz}/\rho}}{\nu \mathcal{R}_t}\right]\right\}, \tag{2}$$

where $\kappa = 0.4$ is von Kármán's constant, τ_{xz} is the bed shear stress, and ρ is the constant fluid density. d is the sand-equivalent roughness size, from which we define the Reynolds number $\mathcal{R}_d = du_*/\nu$. The exponential term in **Eq. 2** suppresses turbulent mixing within the viscous sub-layer close to the bed. The term $r \times d$ corresponds to the standard Prandtl hydrodynamic roughness z_0 extracted by extrapolating the logarithmic law of the wall at vanishing velocity, $u_x = (u_*/\kappa)\ln(z/z_0)$. The term $s \times d$ controls the reduction of the viscous layer thickness upon increasing bed roughness. In the rough limit where $d \propto \mathcal{R}_d \to \infty$, the exponential term vanishes and the hydrodynamic anomaly is suppressed altogether. The dimensionless parameters $r \simeq 1/30$ and $s \simeq 1/3$ are calibrated from measurements of velocity profiles over various rough walls [59, 60].

In **Eq. 2**, $\mathcal{R}_t$ is the van Driest transitional Reynolds number. Following Hanratty [49], the hydrodynamic anomaly is captured by a spatial relaxation of $\mathcal{R}_t$. In the homogeneous case of a flat bed, it is $\mathcal{R}_t^0 \simeq 25$. However, in general, $\mathcal{R}_t$ is not constant but instead trails behind the pressure gradient by a space lag on the order of (ν/u_*) that is associated with a thickening of the boundary layer,

$$(a\nu/u_*)\partial_x \mathcal{R}_t = b\mathcal{R}_t^0 \nu/\left(\rho u_*^3\right)\partial_x\left(\tau_{xx} - p\right) - \left(\mathcal{R}_t - \mathcal{R}_t^0\right). \tag{3}$$

Charru, et al. [27] calibrated this additional equation with $a \simeq 2000$ and $b \simeq 35$ by matching theoretical predictions to basal shear stress measurements [32, 33, 44, 47, 61]. These predictions were obtained in the regime where the hydrodynamic equations could be linearized with respect to $k\zeta$, and then solved for

boundary conditions [9, 10, 51]. In this regime, we write the basal shear stress response $\delta\tau_{xz}$ to the bed perturbation (1) as

$$\delta\tau_{xz}/\rho u_*^2 = k\zeta [-\mathcal{A}\cos(kx) + \mathcal{B}\sin(kx)]. \quad (4)$$

Here, ρu_*^2 is reference shear stress in the flat base state. In **Eq. 4**, the two terms in straight brackets respectively quantify the in-phase and in-quadrature contributions of the response. Both $\mathcal{A}$ and $\mathcal{B}$ have values of order unity [32, 39] and are positive, thereby producing a shear stress leading the bed elevation. They are weak logarithmic functions of the bed wavenumber, except in the range $10^{-4} \leq kz_0 \leq 10^{-2}$ where strong variations arise around the hydrodynamic anomaly [27, 51].

Similarly, we write the basal pressure response δp in the linear regime as

$$\delta p/\rho u_*^2 = k\zeta [-\mathcal{C}\cos(kx) + \mathcal{D}\sin(kx)]. \quad (5)$$

Figure 1 shows how $\mathcal{C}$ and $\mathcal{D}$ vary with the dimensionless wavenumber $k \times z_0$ in the rough $\mathcal{R}_d \gg 1$ and smooth $\mathcal{R}_d \to 0$ limits [9, 10, 51]. The opposite signs $C < 0$ and $D > 0$ mean that, in contrast with shear stress, the phase of pressure modulations are delayed with respect to the bed profile. In addition, because $|\mathcal{C}| \gg \mathcal{D}$, the pressure response is dominated by the Bernoulli effect, in that it is nearly out-of-phase with the topography. Therefore, variations of $\mathcal{C}$ with wavenumber are well captured by approximating the flow as inviscid and irrotational. In this case, the pressure varies as the square of the velocity at a height $\leq \lambda$ on the order of the wavelength, which is the only macroscopic scale over which a pressure disturbance is expected to penetrate the flow. From the logarithmic law of the wall, the velocity therefore scales as $(u_*/\kappa)\ln(b\lambda/z_0)$, where b is ≤ 1. This argument suggests that, in the rough case where complications associated with the hydrodynamic anomaly do not arise, $\mathcal{C}$ should scale as the square of $\ln(kz_0)$. As the parabola in **Figure 1A** shows, this approximation indeed conforms well to the theory for the rough case [9, 10]. The smooth case differs from this log-parabolic behavior above $kz_0 \simeq 10^{-3}$ where the anomaly comes into play. While the dependence of $\mathcal{C}$ flattens somewhat at the larger wavenumbers, the anomaly has a more pronounced effect on $\mathcal{D}$, with a distinctive non-monotonic behavior spanning a decade around $kz_0 \simeq 10^{-3}$ (**Figure 1B**).

3 PRESSURE MEASUREMENTS OVER WAVY SURFACES

In this section, we compare theoretical predictions to available experimental data. We first outline how to fit the recorded pressure profiles. Then, for each set, we discuss how this procedure yields $\mathcal{C}$, $\mathcal{D}$, and their respective uncertainties.

3.1 Fitting Procedure

Because the theory is built on a linear analysis of hydrodynamic equations, we restrict attention to data sets with a harmonic pressure response to topographical variations at low $k\zeta \leq 0.2$ (**Table 1**). However, as **Figure 2** and graphs in **Supplementary Appendix S1** indicate,

relatively weak non-linearities are apparent. Accordingly, we fit dimensionless pressure response profiles to third-order expansions of the form

$$\delta p/\rho u_*^2 = k\zeta [\Delta_1\cos(kx - \phi_1) + \Delta_2\cos(2kx - \phi_2)$$
$$+ \Delta_3\cos(3kx - \phi_3)], \quad (6)$$

but we infer $\mathcal{C}$, $\mathcal{D}$ from the leading order

$$\mathcal{C} = -\Delta_1 \Big/ \sqrt{1 + \tan^2\phi_1}, \quad (7)$$

$$\mathcal{D} = \Delta_1 \tan\phi_1 \Big/ \sqrt{1 + \tan^2\phi_1}. \quad (8)$$

For the data sets under consideration, the second and third terms have amplitudes Δ_2 and $\Delta_3 \ll \Delta_1$. As expected, fitting them to first-order alone ($\Delta_1 \neq 0$, $\Delta_2 = \Delta_3 = 0$) does not significantly affect the resulting $\mathcal{C}$ and $\mathcal{D}$.

Uncertainties in $\mathcal{C}$ and $\mathcal{D}$ depend not only on experimental scatter in Δ_1 and ϕ_1, but also on how u_* was inferred. Using **Eqs 7**, **8**, we estimate uncertainties due to scatter by carrying out a least-squares regression of data to Δ_1 and ϕ_1, while assuming that Δ_1 and ϕ_1 are uncorrelated and normally distributed. Unfortunately, too little information is available to gauge how accurately u_* was established.
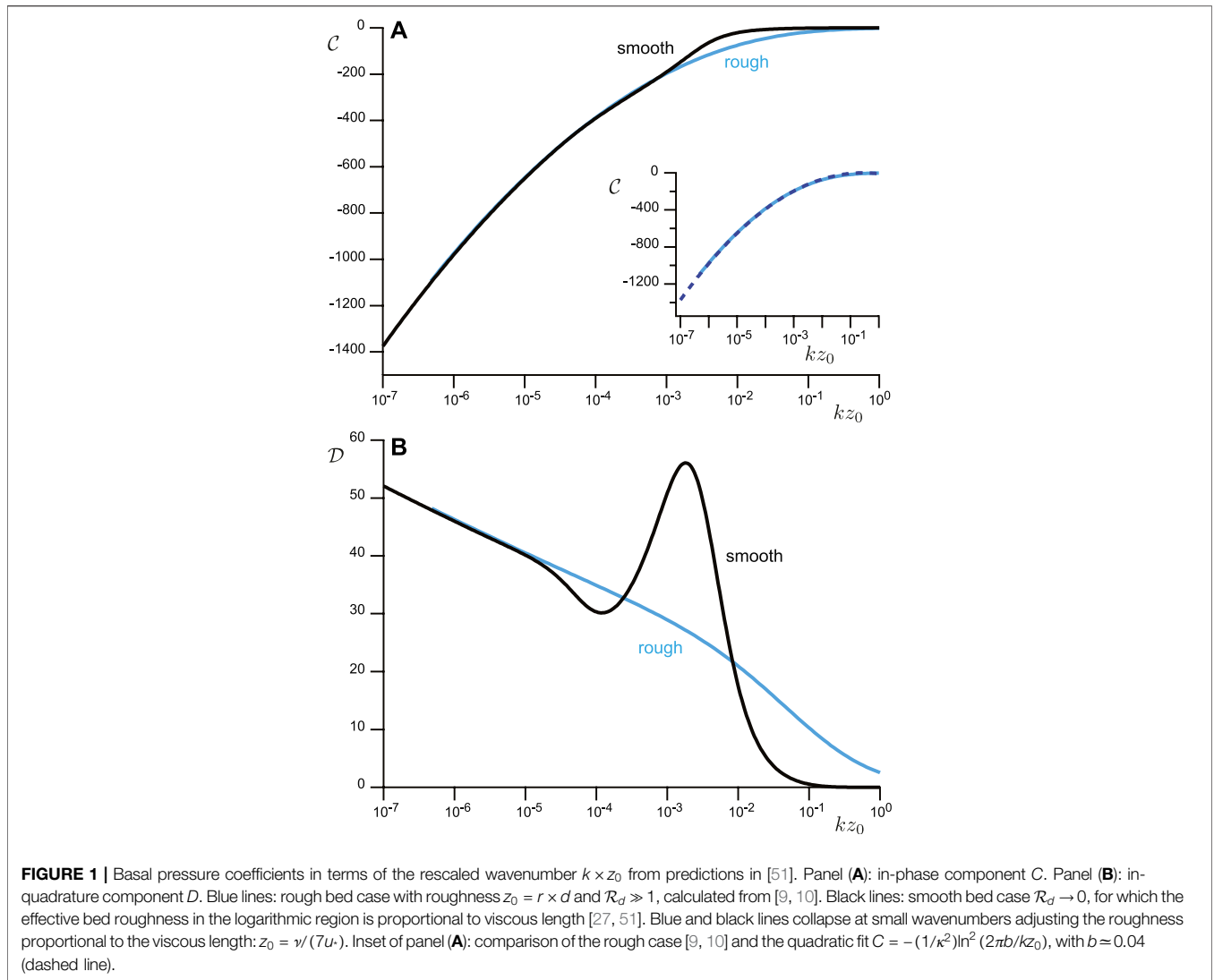
3.2 Zilker et al. and Cook

We first review experiments reported in [47], which were used to compare predictions for basal shear stress and related behavior of $\mathcal{A}$ and $\mathcal{B}$ in [27]. Experiments were conducted in a rectangular channel circulating an electrolyte of density $\rho = 1.02 \times 10^3$ kg/m^3 and kinematic viscosity $\nu = 8.7 \times 10^{-7}$ m^2/s. The bottom of the test section featured interchangeable smooth Plexiglas wavy surfaces of fixed $\lambda = 5.08$ cm but different amplitudes ζ. Basal shear stress and static wall pressure were respectively measured with an electrochemical method and small taps. Shear velocity u_* was inferred from measurements of flow rate by integrating the logarithmic law of the wall recorded on a flat surface.

As **Figure 2** shows for $k\zeta = 0.16$, the pressure profiles exhibit a minimum shortly after the crest. From **Eq. 6**, we find $\mathcal{C} = -193 \pm 4$ and $\mathcal{D} = 35 \pm 4$. Cook [56] measured additional pressure profiles in a similar setup, albeit using another electrolyte solution with $\rho = 1.05 \times 10^3$ kg/m^3 and $\nu = 1.08 \times 10^{-6}$ m^2/s. Data at four different flow rates are shown in **Supplementary Figure S1**. Pressure amplitude increases with flow velocity, whereas phase shift with respect to bed elevation decreases. $\mathcal{D}$ remains nearly constant ~ 40, while $-\mathcal{C}$ rises with u_* (**Table 1**).

3.3 Motzfeld and Kendall

We analyzed experiments performed in wind tunnels over smooth solid sinusoidal waves. The oldest work is Motzfeld's [37], who staged four different bed profiles carved in plaster and varnished. To stay within reach of the linear assumption, we only exploited his data for the smallest amplitude (his 'model I' with $k\zeta = 0.16$ and $\lambda = 0.3$ m). The corresponding pressure profile and fits are shown in **Supplementary Figure S2**. **Eq. 6**

FIGURE 1 | Basal pressure coefficients in terms of the rescaled wavenumber $k \times z_0$ from predictions in [51]. Panel (**A**): in-phase component C. Panel (**B**): in-quadrature component D. Blue lines: rough bed case with roughness $z_0 = r \times d$ and $\mathcal{R}_d \gg 1$, calculated from [9, 10]. Black lines: smooth bed case $\mathcal{R}_d \to 0$, for which the effective bed roughness in the logarithmic region is proportional to viscous length [27, 51]. Blue and black lines collapse at small wavenumbers adjusting the roughness proportional to the viscous length: $z_0 = \nu/(7u_*)$. Inset of panel (**A**): comparison of the rough case [9, 10] and the quadratic fit $C = -(1/\kappa^2)\ln^2(2\pi b/kz_0)$, with $b \simeq 0.04$ (dashed line).

yields a relatively precise $\mathcal{C} = -377 \pm 22$, but a less accurate $\mathcal{D} = 13 \pm 24$, which hints at pressure variations almost in phase with the bed.

The other wind tunnel data are Kendall's [36], who studied turbulent flows over mobile and immobile waves on a rubber surface. We only considered his immobile sinusoidal bed ($k\zeta = 0.2$, $\lambda = 0.1$ m) at different wind velocities. Profiles are shown in **Supplementary Figure S3**. Consistent with the results of [56], Kendall's [36] pressure amplitude increases with flow velocity, while phase with respect to bed elevation decreases.

Motzfeld [37] and Kendall [36] both inferred shear velocity from logarithmic fits of vertical velocity profiles. However, Kendall fitted z_0 and u_* separately. Because hydrodynamic roughness on a smooth wall is correlated with shear velocity, we recalculated Kendall's u_* using $z_0 \simeq \nu/(7u_*)$.

3.4 Musa et al

Musa et al. [29] also acquired data on sinusoidal, smooth, rigid walls in the wind tunnel ($\lambda = 0.1$ m), but their objective was to record pore pressure within a permeable rigid material mimicking a sand bed. We only consider their ripple of smallest amplitude ($k\zeta = 0.19$), which they deployed at six different wind speeds. From a solution of the Laplace equation governing pore pressure, Musa et al. fitted δp at the surface to their pore pressure measurements at 45 locations within the ripple [In the nomenclature of their Eq. 9, $p_1\cos(2\pi x/\lambda - \phi_1)$ is equivalent to our δp]. They then inferred shear velocities by fitting vertical wind profiles to the logarithmic law of the wall using an aerodynamic roughness proportional to the viscous length. For consistency with other data reviewed here, we adopt $z_0 = \nu/(7u_*)$, which differs slightly from their fit of z_0 in the smooth limit. Surface pressure profiles and fits to **Eq. 6** are shown in **Supplementary Figure S4** for their six values of u_*. As

TABLE 1 | Experimental conditions and values of C and D inferred from harmonic fits of pressure profiles using **Eqs 7**, **8**. Last column: downwind shift relative to bed wavelength $\psi_1 = \phi_1/(2\pi)$, calculated from $\tan(2\pi\psi_1) = -D/C$.

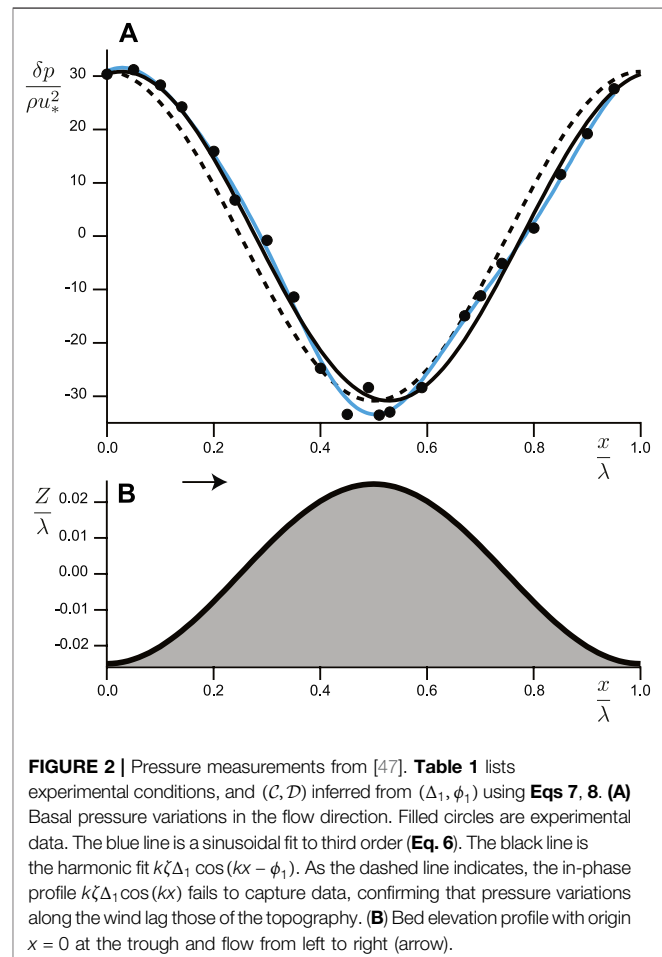| Experiment	Data symbol, bed and fluid properties						
	Profiles	u_* **(m/s)**	$k\nu/u_*$	**C**	**D**	ψ_1 **(%)**
Zilker et al. [47]	•, $\lambda = 0.05$ m, $k\zeta = 0.16$, $\nu = 8.7 \times 10^{-7}$ m^2/s, $\rho = 1.02 \times 10^3$ kg/m^3					
	Figure 2A	0.028	0.0038	−193 ± 4	35 ± 4	2.8 ± 0.4
Cook [56]	◦, $\lambda = 0.05$ m, $k\zeta = 0.16$, $\nu = 1.08 \times 10^{-6}$ m^2/s, $\rho = 1.05 \times 10^3$ kg/m^3					
	Supplementary Figure S1A	0.030	0.0045	−140 ± 3	41 ± 3	4.5 ± 0.4
	Supplementary Figure S1B	0.062	0.0022	−217 ± 3	42 ± 3	3.0 ± 0.3
	Supplementary Figure S1C	0.076	0.0018	−231 ± 2	37 ± 2	2.5 ± 0.2
	Supplementary Figure S1D	0.079	0.0017	−246 ± 2	41 ± 2	2.6 ± 0.1
Motzfeld [37]	▲, $\lambda = 0.3$ m, $k\zeta = 0.16$, $\nu = 1.5 \times 10^{-5}$ m^2/s, $\rho = 1.2$ kg/m^3					
	Supplementary Figure S2	0.69	0.0005	−377 ± 22	13 ± 24	0.5 ± 1.0
Kendall [36]	■, $\lambda = 0.1$ m, $k\zeta = 0.2$, $\nu = 1.5 \times 10^{-5}$ m^2/s, $\rho = 1.2$ kg/m^3					
	Supplementary Figure S3A	0.13	0.0072	−135 ± 1	51 ± 1	5.7 ± 0.2
	Supplementary Figure S3B	0.21	0.0044	−166 ± 1	46 ± 1	4.3 ± 0.1
	Supplementary Figure S3C	0.30	0.0031	−193 ± 1	41 ± 1	3.3 ± 0.1
	Supplementary Figure S3D	0.39	0.0024	−225 ± 1	38 ± 1	2.6 ± 0.1
Musa et al. [29]	◇, $\lambda = 0.1$ m, $k\zeta = 0.19$, $\nu = 1.5 \times 10^{-5}$ m^2/s, $\rho = 1.2$ kg/m^3					
	Supplementary Figure S4A	0.16	0.0058	−225 ± 11	78 ± 13	5.3 ± 1.1
	Supplementary Figure S4B	0.33	0.0028	−284 ± 11	59 ± 13	3.2 ± 0.8
	Supplementary Figure S4C	0.55	0.0017	−256 ± 10	38 ± 12	2.3 ± 0.8
	Supplementary Figure S4D	0.76	0.0012	−241 ± 10	45 ± 12	2.9 ± 0.9
	Supplementary Figure S4E	0.95	0.0010	−258 ± 11	48 ± 13	2.9 ± 0.9
	Supplementary Figure S4F	1.21	0.0008	−252 ± 11	50 ± 12	3.1 ± 0.9

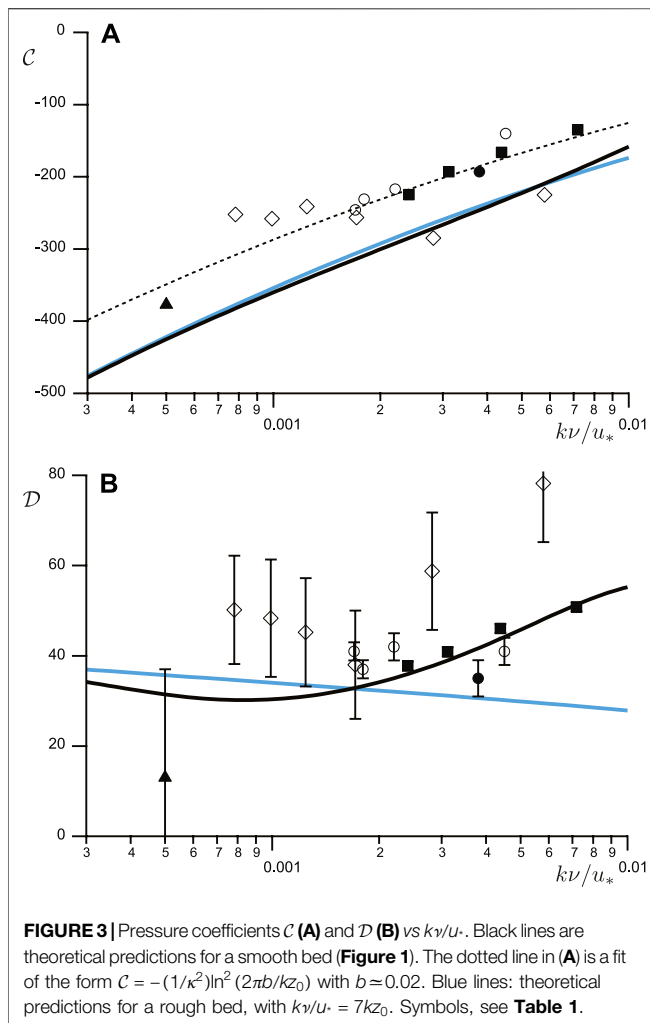the open diamonds in **Figure 3** suggest, $-\mathcal{C}$ rose slowly with u_* and $\mathcal{D}$ was non-monotonic.

4 DISCUSSION AND CONCLUDING REMARKS

Table 1 summarizes conditions of all available experiments on smooth walls with nearly harmonic response, and the resulting $\mathcal{C}$ and $\mathcal{D}$. First- and third-order fits of experimental pressure profiles yield similar values for these quantities, thereby demonstrating robustness of the fitting procedure. Uncertainties are relatively small, except for $\mathcal{D}$ from Motzfeld and from Musa, et al.

Figure 3 shows corresponding variations with the rescaled wavenumber $k\nu/u_*$ and, consistently with experimental conditions, compares them with theoretical predictions in the smooth case [9, 10, 51], which rely on a calibration of the hydrodynamic equations and the relaxation framework of Hanratty [49] on the streamwise evolution of basal shear stress [27]. While these preditions capture the correct trend, they clearly underpredict $\mathcal{C}$. A Bernoulli-like approximation (dotted line in **Figure 3A**) is more faithful to the data, but it requires $b \sim 0.02$, which is lower than the value used in the inset of **Figure 1** by a factor of 2. We attribute the discrepancy to challenges in extracting u_* from experiments.

At first glance, **Figure 3** suggests that $\mathcal{D}$ is nearly constant within experimental error. However, its trend vs $k\nu/u_*$ hints at the presence of a local minimum from the hydrodynamic anomaly for a smooth wall (black curve in **Figure 1**). Nonetheless, the precision in $\mathcal{D}$ is not yet sufficient to distinguish this behavior from that of a rough wall (blue curve).

FIGURE 2 | Pressure measurements from [47]. **Table 1** lists experimental conditions, and $(\mathcal{C}, \mathcal{D})$ inferred from (Δ_1, ϕ_1) using **Eqs 7**, **8**. **(A)** Basal pressure variations in the flow direction. Filled circles are experimental data. The blue line is a sinusoidal fit to third order (**Eq. 6**). The black line is the harmonic fit $k\zeta\Delta_1 \cos(kx - \phi_1)$. As the dashed line indicates, the in-phase profile $k\zeta\Delta_1 \cos(kx)$ fails to capture data, confirming that pressure variations along the wind lag those of the topography. **(B)** Bed elevation profile with origin $x = 0$ at the trough and flow from left to right (arrow).

FIGURE 3 | Pressure coefficients $\mathcal{C}$ **(A)** and $\mathcal{D}$ **(B)** vs $k\nu/u_*$. Black lines are theoretical predictions for a smooth bed (**Figure 1**). The dotted line in (**A**) is a fit of the form $\mathcal{C} = -(1/\kappa^2)\ln^2(2\pi b/kz_0)$ with $b \simeq 0.02$. Blue lines: theoretical predictions for a rough bed, with $k\nu/u_* = 7kz_0$. Symbols, see **Table 1**.

Overall, $\mathcal{C}$ and $\mathcal{D}$ exhibit dispersion among different experiments. One reason is inconsistent ways to evaluate u_*, which affects both axes in **Figure 3** by rescaling stresses with ρu_*^2 and lengths with ν/u_*. Because velocity fluctuations or Reynolds stresses close to the bed are difficult to measure, u_* was inferred from velocity profiles or flow rates using the law of the wall. In addition, it is open to question how flows driven by a pressure gradient, such as those in wind tunnels or pipes, can be quantitatively compared to a theoretical framework where shear stress is imposed. In this context, the Bernoulli-like approximation suggests that the velocity very close to the bed at an altitude $\simeq b\lambda$ is a better proxy for an effective u_* than the average flow velocity.

A second issue is non-linear effects. Weakly non-linear developments [9, 62] and measurements [10] suggest that $k\zeta = 0.2$ is an upper bound for validity of the linear theory. In recorded pressure profiles, we clearly discern weakly non-linear effects, especially in Musa et al. (**Supplementary Figure S4**), whose pressure is lower than expected on bed crests and troughs, although this effect may be due to an interaction with the porous bed underneath [29]. In addition, non-linearities also raise the effective bed roughness on a scale comparable to λ, with

a first corrective term in $(k\zeta)^2$ [9]. This further complicates an estimation of the relevant experimental shear velocity.

These observations call for more measurements, particularly in the range $10^{-3} \lesssim k\nu/u_* \lesssim 10^{-1}$ that resolves the peak of the hydrodynamic anomaly. For air at ordinary wind speed, for example $u_* \simeq 0.5$ m/s, this implies a wavy bed with $2\,\text{mm} < \lambda < 20\,\text{cm}$. For more gentle winds, the smaller wavelength could rise to 1 cm. Larger λ could be staged with oils of larger viscosity. Data at significantly smaller wavenumbers would require a natural wavy surface such as a sand dune. An example is the hump studied in [32], where $\lambda \simeq 40$ m and $kz_0 \simeq 10^{-5}$ in the rough limit. Here, the theory predicts $\mathcal{C} \simeq -700$ and $\mathcal{D} \simeq 40$, i.e. a phase shift $\phi_1 \simeq 0.06$ rad, corresponding to a distance $\phi_1/k \simeq 0.4$ m downwind of the crest. If small pressure differences could be reliably recorded over relatively long distances, such spatial phase lag could also be measured.

Finally, DNS or LES simulations would also constitute another source of data, since runs could be performed with strictly imposed values of u_* [63, 64], thereby mirroring the theoretical approach. Unfortunately, simulations of Maaß and Schumann [65, 66] or those of Salvetti et al. [67] involve amplitudes too large to avoid non-linear effects arising at $k\zeta \gtrsim 0.1$. In both experimental and numerical investigations, $k\nu/u_*$ is typically adjusted at fixed wavenumber using different winds. However, investigating the role of k under constant flow is equally valuable, perhaps again with DNS, to gain a deeper understanding of the hydrodynamic anomaly. At present, the relaxation closure inspired from Hanratty [49] is convenient. However, the interplay between a wavy bed and modulation of the viscous sublayer remains an open problem.

The evolution of pressure on geophysical bedforms such as sand ripples creates an internal seepage flow that brings nutrients to the liveforms they shelter [68], and it provides a mechanism for the accumulation of moisture or dust within them [28]. The phase lag that is proportional to $\arctan(\mathcal{D}/\mathcal{C}) < 0$ also induces surface variations that future research could relate to complex drying patterns that are observed in sand seas [69]. More generally, pressure variations affect phase change and thermodynamics. Pressure is also a stress scale that may alter the rheology of dense granular flows and suspensions in subtle ways, for example by altering the opening and closing of contacts among grains [70], especially when the continuous phase is a liquid [72]. Although initially motivated by wind flows over ripple-like bed oscillations, the pressure effects that we have reviewed could then be relevant to subjects as diverse as dissolution and sublimation patterns [50, 51, 72], granular soil liquefaction [71], droplets and aerosols production [73] and cloud formation over larger scale topography [30, 31].

DATA AVAILABILITY STATEMENT

Publicly available datasets were analyzed in this study. This data can be found here: The data are available in the cited references.

AUTHOR CONTRIBUTIONS

All authors contributed equally to this work.

SUPPLEMENTARY MATERIAL

The Supplementary Material for this article can be found online at: https://www.frontiersin.org/articles/10.3389/fphy.2021.682564/full#supplementary-material

REFERENCES

1. Jackson PS, and Hunt JCR. Turbulent Wind Flow over a Low Hill. *Q.J R Met. Soc.* (1975) 101:929–55. doi:10.1002/qj.49710143015

2. Benjamin TB. Shearing Flow over a Wavy Boundary. *J Fluid Mech* (1959) 6: 161–205. doi:10.1017/s0022112059000568

3. Bordner GL. Nonlinear Analysis of Laminar Boundary Layer Flow over a Periodic Wavy Surface. *Phys Fluids* (1978) 21:1471–64. doi:10.1063/1.862409

4. Buckles J, Hanratty TJ, and Adrian RJ. Turbulent Flow over Large-Amplitude Wavy Surfaces. *J Fluid Mech* (1984) 140:27–44. doi:10.1017/s0022112084000495

5. Caponi EA, Fornberg B, Knight DD, McLean JW, Saffman PG, and Yuen HC. Calculations of Laminar Viscous Flow over a Moving Wavy Surface. *J Fluid Mech* (1982) 124:247–62. doi:10.1017/s0022112082002535

6. Lagrée P-Y. A Triple Deck Model of Ripple Formation and Evolution. *Phys Fluids* (2003) 15:2355–68. doi:10.1063/1.1588305

7. Belcher SE, and Hunt JCR. Turbulent Flow over Hills and Waves. *Annu Rev Fluid Mech* (1998) 30:507–38. doi:10.1146/annurev.fluid.30.1.507

8. Britter RE, Hunt JCR, and Richards KJ. Air Flow over a Two-Dimensional Hill: Studies of Velocity Speed-Up, Roughness Effects and Turbulence. *Q.J.R Meteorol Soc* (1981) 107:91–110. doi:10.1002/qj.49710745106

9. Fourrière A. *Morphodynamique des rivières, sélection de largeur, rides et dunes (River morphodynamics : Width selection, ripples and dunes)*. Ph.D. thesis: Université Paris Diderot (2009). Available from: https://pastel.archives-ouvertes.fr/pastel-00005562 (Accessed March 2, 2009).

10. Fourrière A, Claudin P, and Andreotti B. Bedforms in a Turbulent Stream: Formation of Ripples by Primary Linear Instability and of Dunes by Nonlinear Pattern Coarsening. *J Fluid Mech* (2010) 649:287–328. doi:10.1017/s0022112009993466

11. Hunt JCR, Leibovich S, and Richards KJ. Turbulent Shear Flows over Low Hills. *Q.J R Met. Soc.* (1988) 114:1435–70. doi:10.1002/qj.49711448405

12. Kobayashi N, and Madsen OS. Turbulent Flows over a Wavy Bed. *J Geophys Res* (1985) 90:7323–31. doi:10.1029/jc090ic04p07323

13. Kroy K, Sauermann G, and Herrmann HJ. Minimal Model for Aeolian Sand Dunes. *Phys Rev E* (2002) 66:031302. doi:10.1103/physreve.66.031302

14. Luchini P, and Charru F. Quasilaminar Regime in the Linear Response of a Turbulent Flow to Wall Waviness. *Phys Rev Fluids* (2017) 2(R):012601. doi:10.1103/physrevfluids.2.012601

15. Sykes RI. An Asymptotic Theory of Incompressible Turbulent Boundarylayer Flow over a Small Hump. *J Fluid Mech* (1980) 101:647–70. doi:10.1017/s002211208000184x

16. Taylor PA. Some Numerical Studies of Surface Boundary-Layer Flow above Gentle Topography. *Boundary-layer Meteorol* (1977) 11:439–65. doi:10.1007/bf02185870

17. Taylor PA. Numerical Studies of Neutrally Stratified Planetary Boundary-Layer Flow above Gentle Topography. *Boundary-layer Meteorol* (1977) 12: 37–60. doi:10.1007/bf00116397

18. Taylor PA, Mason PJ, and Bradley EF. Boundary-layer Flow over Low Hills. *Boundary-layer Meteorol* (1987) 39:107–32. doi:10.1007/bf00121870

19. Finnigan J, Ayotte K, Harman I, Katul G, Oldroyd H, Patton E, et al. Boundary-layer Flow over Complex Topography. *Boundary-layer Meteorol* (2020) 177: 247–313. doi:10.1007/s10546-020-00564-3

20. Paquier A, Moisy F, and Rabaud M. Viscosity Effects in Wind Wave Generation. *Phys Rev Fluids* (2016) 1:083901. doi:10.1103/physrevfluids.1.083901

21. Sullivan PP, and McWilliams JC. Dynamics of Winds and Currents Coupled to Surface Waves. *Annu Rev Fluid Mech* (2010) 42:19–42. doi:10.1146/annurev-fluid-121108-145541

22. Hansen RJ, Hunston DL, Ni CC, and Reischman MM. An Experimental Study of Flow-Generated Waves on a Flexible Surface. *J Sound Vibration* (1980) 68: 317–34. doi:10.1016/0022-460x(80)90389-2

23. Jia P, Andreotti B, and Claudin P. Paper Waves in the Wind. *Phys Fluids* (2015) 27:104101. doi:10.1063/1.4931777

24. Zhang C, Wang J, Blake W, and Katz J. Deformation of a Compliant Wall in a Turbulent Channel Flow. *J Fluid Mech* (2017) 823:345–90. doi:10.1017/jfm.2017.299

25. Shelley MJ, and Zhang J. Flapping and Bending Bodies Interacting with Fluid Flows. *Annu Rev Fluid Mech* (2011) 43:449–65. doi:10.1146/annurev-fluid-121108-145456

26. Shields A. *Anwendung der Aehnlichkeitsmechanik und der Turbulenzforschung auf die Geschiebebewegung (Application of similarity principles and turbulence research to bedload motion)*. Berlin: Mitteilungen der Preußischen Versuchsanstalt für Wasserbau (1936) 26. p. 1–26.

27. Charru F, Andreotti B, and Claudin P. Sand Ripples and Dunes. *Annu Rev Fluid Mech* (2013) 45:469–93. doi:10.1146/annurev-fluid-011212-140806

28. Louge MY, Valance A, Mint Babah H, Moreau-Trouvé J-C, Ould el-Moctar A, Dupont P, et al. Seepage-induced Penetration of Water Vapor and Dust beneath Ripples and Dunes. *J Geophys Res* (2010) 115:F02002. doi:10.1029/2009jf001385

29. Musa RA, Takarrouht S, Louge MY, Xu J, and Berberich ME. Pore Pressure in a Wind-Swept Rippled Bed below the Suspension Threshold. *J Geophys Res* (2014) 119:2475–590. doi:10.1002/2014jf003293

30. Smith RB. The Influence of Mountains on the Atmosphere. *Adv Geophys* (1979) 21:87–230. doi:10.1016/s0065-2687(08)60262-9

31. Whiteman CD. *Mountain Meteorology*. Oxford University Press (2000). doi:10.1093/oso/9780195132717.003.0015

32. Claudin P, Wiggs GFS, and Andreotti B. Field Evidence for the Upwind Velocity Shift at the Crest of Low Dunes. *Boundary-layer Meteorol* (2013) 148: 195–206. doi:10.1007/s10546-013-9804-3

33. Finnigan JJ, Raupach MR, Bradley EF, and Aldis GK. A Wind Tunnel Study of Turbulent Flow over a Two-Dimensional Ridge. *Boundary-layer Meteorol* (1990) 50:277–317. doi:10.1007/bf00120527

34. Gong W, and Ibbetson A. A Wind Tunnel Study of Turbulent Flow over Model Hills. *Boundary-layer Meteorol* (1989) 49:113–48. doi:10.1007/bf00116408

35. Gong W, Taylor PA, and Dörnbrack A. Turbulent Boundary-Layer Flow over Fixed Aerodynamically Rough Two-Dimensional Sinusoidal Waves. *J Fluid Mech* (1996) 312:1–37. doi:10.1017/s0022112096001905

36. Kendall JM. The Turbulent Boundary Layer over a Wall with Progressive Surface Waves. *J Fluid Mech* (1970) 41:259–81. doi:10.1017/s0022112070000617

37. Motzfeld H. Die Turbulente Strömung an Welligen Wänden. *Z Angew Math Mech* (1937) 17:193–212. doi:10.1002/zamm.19370170402

38. Weng WS, Hunt JCR, Carruthers DJ, Warren A, Wiggs GFS, Livingstone I, et al. Air Flow and Sand Transport over Sand-Dunes. *Acta Mechanica* (1991) 2: 1–22. doi:10.1007/978-3-7091-6703-8_1

39. Lü P, Narteau C, Dong Z, Claudin P, Rodriguez S, An Z, et al. Direct Validation of Dune Instability Theory. *Proc Natl Acad Sci USA* (2021) 118:e2024105118. doi:10.1073/pnas.2024105118

40. Abrams J, and Hanratty TJ. Relaxation Effects Observed for Turbulent Flow over a Wavy Surface. *J Fluid Mech* (1985) 151:443–55. doi:10.1017/s0022112085001045

41. Haward SJ, Shen AQ, Page J, and Zaki TA. Poisseuille Flow over a Wavy Surface. *Phys Rev Fluids* (2017) 12:124102. doi:10.1103/PhysRevFluids.2.124102

42. Nakagawa S, and Hanratty TJ. Particle Image Velocimetry Measurements of Flow over a Wavy Wall. *Phys Fluids* (2001) 13:3504–7. doi:10.1063/1.1399291

43. Nelson JM, McLean SR, and Wolfe SR. Mean Flow and Turbulence Fields over Two-Dimensional Bed Forms. *Water Resour Res* (1993) 29:3935–53. doi:10.1029/93wr01932

44. Poggi D, Katul GG, Albertson JD, and Ridolfi L. An Experimental Investigation of Turbulent Flows over a Hilly Surface. *Phys Fluids* (2007) 19:036601. doi:10.1063/1.2565528

45. Venditti JG. Turbulent Flow and Drag over Fixed Two- and Three-Dimensional Dunes. *J Geophys Res* (2007) 112:F04008. doi:10.1029/2006jf000650

46. Wiberg PL, and Nelson JM. Unidirectional Flow over Asymmetric and Symmetric Ripples. *J Geophys Res* (1992) 97:12745–61. doi:10.1029/92jc01228

47. Zilker DP, Cook GW, and Hanratty TJ. Influence of the Amplitude of a Solid Wavy Wall on a Turbulent Flow. Part 1. Non-separated Flows. *J Fluid Mech* (1977) 82:29–51. doi:10.1017/s0022112077000524

48. Zilker DP, and Hanratty TJ. Influence of the Amplitude of a Solid Wavy Wall on a Turbulent Flow. Part 2. Separated Flows. *J Fluid Mech* (1979) 90:257–71. doi:10.1017/s0022112079002196

49. Hanratty TJ. Stability of Surfaces that Are Dissolving or Being Formed by Convective Diffusion. *Annu Rev Fluid Mech* (1981) 13:231–52. doi:10.1146/annurev.fl.13.010181.001311

50. Meakin P, and Jamtveit B. Geological Pattern Formation by Growth and Dissolution in Aqueous Systems. *Proc R Soc A* (2010) 466:659–94. doi:10.1098/rspa.2009.0189

51. Claudin P, Durán O, and Andreotti B. Dissolution Instability and Roughening Transition. *J Fluid Mech* (2017) 832:R2. doi:10.1017/jfm.2017.711

52. Bordiec M, Carpy S, Bourgeois O, Herny C, Massé M, Perret L, et al. Sublimation Waves: Geomorphic Markers of Interactions between Icy Planetary Surfaces and Winds. *Earth-Science Rev* (2020) 211:103350. doi:10.1016/j.earscirev.2020.103350

53. Bintanja R, Reijmer CH, and Hulscher SJMH. Detailed Observations of the Rippled Surface of Antarctic Blue-Ice Areas. *J Glaciol* (2001) 47:387–96. doi:10.3189/172756501781832106

54. Thomas RM. Size of Scallops and Ripples Formed by Flowing Water. *Nature* (1979) 277:281–3. doi:10.1038/277281a0

55. Durán O, Andreotti B, Claudin P, and Winter C. A Unified Model of Ripples and Dunes in Water and Planetary Environments. *Nat Geosci* (2019) 12:345–50. doi:10.1038/s41561-019-0336-4

56. Cook GW. *Turbulent Flow over Solid Wavy Surfaces*. PhD thesis. Urbana-Champaign, IL: University of Illinois at Urbana-Champaign (1970).

57. Pope SB. *Turbulent Flows*. Cambridge, United Kingdom: Cambridge Univ. Press (2000). doi:10.1017/cbo9780511840531

58. van Driest ER. On Turbulent Flow Near a Wall. *J Aeronaut Sci* (1956) 23:1007–11. doi:10.2514/8.3713

59. Flack KA, and Schultz MP. Review of Hydraulic Roughness Scales in the Fully Rough Regime. *J Fluid Eng* (2010) 132:041203. doi:10.1115/1.4001492

60. Schultz MP, and Flack KA. Turbulent Boundary Layers on a Systematically Varied Rough Wall. *Phys Fluids* (2009) 21:015104. doi:10.1063/1.3059630

61. Frederick KA, and Hanratty TJ. Velocity Measurements for a Turbulent Nonseparated Flow over Solid Waves. *Experiments in Fluids* (1988) 6:477–86. doi:10.1007/bf00196509

62. Andreotti B, Fourrière A, Ould-Kaddour F, Murray B, and Claudin P. Giant Aeolian Dune Size Determined by the Average Depth of the Atmospheric Boundary Layer. *Nature* (2009) 457:1120–3. doi:10.1038/nature07787

63. de Angelis V, Lombardi P, and Banerjee S. Direct Numerical Simulation of Turbulent Flow over a Wavy Wall. *Phys Fluids* (1997) 9:2429–42. doi:10.1063/1.869363

64. Henn DS, and Sykes RI. Large-eddy Simulation of Flow over Wavy Surfaces. *J Fluid Mech* (1999) 383:75–112. doi:10.1017/s0022112098003723

65. Maaß C, Schumann U, Voke PR, Kleiser L, and Chollet JP. *Numerical Simulation of Turbulent Flow over a Wavy Boundary. Direct and Large Eddy Simulation*. Dordrecht, The Netherlands: Kluwer (1994). p. 287–97.

66. Maaß C, and Schumann U. Direct Numerical Simulation of Separated Turbulent Flow over a Wavy Boundary, editor EH Hirschel (1996). p. 227–41. doi:10.1007/978-3-322-89849-4_17

67. Salvetti MV, Damiani R, and Beux F. Three-dimensional Coarse Large-Eddy Simulations of the Flow above Two-Dimensional Sinusoidal Waves. *Int J Numer Meth Fluids* (2001) 35:617–42. doi:10.1002/1097-0363(20010330)35:6<617::aid-fld104>3.0.co;2-m

68. Meysman FJR, Galaktionov OS, Cook PLM, Janssen F, Huettel M, and Middelburg JJ. Quantifying Biologically and Physically Induced Flow and Tracer Dynamics in Permeable Sediments. *Biogeosciences* (2007) 4:627–46. doi:10.5194/bg-4-627-2007

69. Louge MY, Valance A, Ould el-Moctar A, Xu J, Hay AG, and Richer R. Temperature and Humidity within a Mobile Barchan Sand Dune, Implications for Microbial Survival. *J Geophys Res* (2013) 118:627–46. doi:10.1002/2013jf002839

70. Tournat V, Zaitsev V, Gusev V, Nazarov V, Béquin P, and Castagnède B. Probing Weak Forces in Granular Media through Nonlinear Dynamic Dilatancy: Clapping Contacts and Polarization Anisotropy. *Phys Rev Lett* (2004) 92:085502. doi:10.1103/physrevlett.92.085502

72. Claudin P, Jarry H, Vignoles G, Plapp M, and Andreotti B. Physical Processes Causing the Formation of Penitentes. *Phys Rev E* (2015) 92:033015. doi:10.1103/physreve.92.033015

71. Andreotti B, Forterre Y, and Pouliquen O. *Granular Media, between Fluid and Solid*. Cambridge University Press (2013). doi:10.1017/cbo9781139541008

73. Villermaux E. Fragmentation. *Annu Rev Fluid Mech* (2007) 39:419–46. doi:10.1146/annurev.fluid.39.050905.110214

Conflict of Interest: The authors declare that the research was conducted in the absence of any commercial or financial relationships that could be construed as a potential conflict of interest.